Inverse modelling of CF_4 and NF_3 emissions in East Asia

Tim Arnold[1,2,3*], Alistair J. Manning[3], Jooil Kim[4], Shanlan Li[5], Helen Webster[3], David Thomson[3], Jens Mühle[4], Ray F. Weiss[4], Sunyoung Park[5,6], and Simon O'Doherty[7]

[1]National Physical Laboratory, Teddington, Middlesex, UK

[2]School of GeoSciences, University of Edinburgh, Edinburgh, UK

[3]Met Office, Exeter, UK

[4]Scripps Institution of Oceanography, University of California, San Diego, La Jolla,

10   California 92037, USA

[5]Kyungpook Institute of Oceanography, Kyungpook National University, Daegu 41566, Republic of Korea

[6]Department of Oceanography, Kyungpook National University, Daegu 41566, Republic of Korea

15   [7]School of Chemistry, University of Bristol, Bristol, UK.

*Corresponding author tim.arnold@ed.ac.uk

Decadal trends in the atmospheric abundances of carbon tetrafluoride (CF_4) and nitrogen trifluoride (NF_3) have been well characterised and have provided a time series of global total
20   emissions. Information on locations of emissions contributing to the global total, however, is currently poor. We use a unique set of measurements between 2008 and 2015 from the Gosan station, Jeju Island, South Korea (part of the Advanced Global Atmospheric Gases Experiment network), together with an atmospheric transport model to make spatially disaggregated emission estimates of these gases in East Asia. Owing to the poor availability
25   of good prior information for this study our emissions estimates are largely influenced by the atmospheric measurements. Notably, we are able to highlight emissions hotspots of NF_3 and CF_4 in South Korea, owing to the measurement location. We calculate emissions of CF_4 to be quite constant between years 2008 and 2015 for both China and South Korea with 2015 emissions calculated at 4.3 ± 2.7 Gg yr^{-1} and 0.36 ± 0.11 Gg yr^{-1}, respectively. Emission

30   estimates of NF_3 from South Korea could be made with relatively small uncertainty at 0.6 ± 0.07 Gg yr^{-1} in 2015, which equates to ~1.6% of the country's CO_2 emissions. We also apply our method to calculate emissions of CHF_3 (HFC-23) between 2008 and 2012, for which our results find good agreement with other studies and which helps support our choice in methodology for CF_4 and NF_3.

1. Introduction

The major greenhouse gases (GHGs) − carbon dioxide, methane and nitrous oxide − have natural and anthropogenic sources. The synthetic fluorinated species (chlorofluorocarbons, hydrochlorofluorocarbons, hydrofluorocarbons, and perfluorocarbons) are almost or entirely anthropogenic and are released from industrial and domestic appliances and applications. Of the synthetic species, tetrafluoromethane (CF_4) and nitrogen trifluoride (NF_3) are emitted nearly exclusively from point sources of specialized industries (Arnold et al., 2013; Mühle et al., 2010). Although these species currently make up only a small percentage of current emissions contributing to global radiative forcing, they have potential to form large portions of specific company, sector, state, province, or even country level GHG budgets.

CF_4 is the longest-lived GHG gas known with an estimated lifetime of 50,000 years, leading to a global warming potential on a 100-year time scale (GWP_{100}) of 6630 (Myhre et al., 2013). Significant increases in atmospheric concentrations are ascribed mainly to emissions from primary aluminum production during so-called "anode events" when the alumina feed to the reduction cell is restricted (International Aluminium Institute, 2016), and from the microchip-manufacturing component of the semiconductor industry (Illuzzi and Thewissen, 2010). Recently, evidence is emerging that, similar to primary aluminium production, rare earth element production may also release substantial amounts of CF_4 (Vogel et al., 2017; Zhang et al., 2017). Other emission sources for CF_4 include release during the production of SF_6 and HCFC-22, but emissions from these sources are estimated to be small compared to the emissions from the aluminium production and semiconductor manufacturing industries (EC-JRC/PBL, 2013; Mühle et al., 2010). There is also a very small natural emission source of CF_4, sufficient to maintain the preindustrial atmospheric burden (Deeds et al., 2008).

According to the IPCC fifth assessment, NF_3's global warming potential on a 100-year time scale (GWP_{100}) is ~16,100 (based on an atmospheric lifetime of 500 years) (Myhre et al., 2013), however, recent work suggests the GWP_{100} is higher at 19,700 owing to an increased estimate in the radiative efficiency (Totterdill et al., 2016). Use of NF_3 began in the 1960s in

specialty applications, e.g., as a rocket fuel oxidizer and as a fluorine donor for chemical lasers (Bronfin and Hazlett, 1966). Beginning in the late 1990s, NF_3 has been used by the semiconductor industry, and in the production of photovoltaic cells and flat-panel displays.

65 NF_3 can be broken down into reactive fluorine (F) radicals and ions, which are used to remove the remaining silicon-containing deposits in process chambers (Henderson and Woytek, 1994; Johnson et al., 2000). NF_3 was also chosen because of its promise as an environmentally friendly alternative, with conversion efficiencies to create reactive F far higher than other compounds such as C_2F_6 (Johnson et al., 2000; International SEMATECH

70 Manufacturing Initiative, 2005). Given its rapid recent rise in the global atmosphere and projected future market, it has been estimated that NF_3 could become the fastest growing contributor to radiative forcing of all the synthetic GHGs by 2050 (Rigby et al., 2014b).

CF_4 and NF_3 are not the only species with major point source emissions. Trifluoromethane $(CHF_3;$ HFC-23) is principally made as a byproduct in the production of

75 chlorodifluoromethane $(CHClF_2,$ HCFC-22). Of the hydrofluorocarbons (HFCs), HFC-23 has the highest 100-year global warming potential (GWP_{100}) at 12,400 owing most significantly to a long atmospheric lifetime of 222 years (Myhre et al., 2013). Its regional and global emissions have been the subject of numerous previous studies (Fang et al., 2014; McCulloch and Lindley, 2007; Miller et al., 2010; Montzka et al., 2010; Fang et al., 2015; Stohl et al.,

80 2010; Li et al., 2011; Kim et al., 2010; Yao et al., 2012; Keller et al., 2012; Yokouchi et al., 2006; Simmonds et al., 2018). Thus, emissions of HFC-23 are already relatively well characterized from a bottom up and top-down perspective. In this work we will also calculate HFC-23 emissions, not to add to current knowledge, but to provide a level of confidence for our methodology.

85 Unlike for HFC-23, the spatial distribution of emissions responsible for CF_4 and NF_3 abundances is very poorly understood, which is hindering action for targeting mitigation. HFC-23 is emitted from well-known sources (namely HCFC-22 production sites) with well characterized estimates of emission magnitudes and hence it has been a target for successful mitigation (by thermal destruction) via the clean development mechanism (Miller et al.,

90 2010). However, emissions of CF_4 and NF_3 are very difficult to estimate from industry level information: Emissions from Al production are highly variable depending on the conditions of manufacturing, and emissions from the electronics industry depend on what is being manufactured, the company's recipes for production (such information is not publicly available), and whether abatement methods are used and how efficient these are under real

95   conditions. Both the Al production and semiconductor industries have launched voluntary

efforts to control their emissions of these substances, reporting success in meeting their goals

(International Aluminium Institute, 2016; Illuzzi and Thewissen, 2010; World Semiconductor

Council, 2017). Despite the industry's efforts to reduce emissions, top-down studies on the

emissions of CF_4 and NF_3 have shown the bottom-up inventories are likely to be highly

100   inaccurate. Most recently, Kim et al. (2014) showed that global bottom-up estimates for CF_4

are as much as 50% lower than top-down estimates, and Arnold et al. (2013) show that the

best estimates of global NF_3 emissions calculated from industry information and statistical

data total only ~35% of that estimated from atmospheric measurements.

Accurate emission estimates of NF_3 and CF_4 are difficult to make based on simple parameters

105   such as integrated country level uptake rates and leakage rates, which, for example, underpin

calculations of HFC emissions. Active or passive activities to reduce emissions vary between

countries, and between industries and companies within countries, and the impetus to

accurately understand emissions is lacking in regions that have not been required to report

emissions under the UNFCCC. This problem is compounded by the difficulty in making

110   measurements of these gases: CF_4 and NF_3 are the two most volatile GHGs after methane,

and have very low atmospheric abundances, which makes routine measurements in the field

at the required precision particularly difficult. The Advanced Global Atmospheric Gases

Experiment (AGAGE) has been monitoring the global atmospheric trace gas budget for

decades (Prinn et al., 2018). Most recently, AGAGE's 'Medusa' pre-concentration GC-MS

115   (gas chromatography-mass spectrometry) system has been able to measure a full suite of the

long-lived halogenated GHGs (Arnold et al., 2012; Miller et al., 2008). The Medusa is the

only instrument demonstrated to measure NF_3 in ambient air samples, and the only field-

deployable instrument capable of measuring CF_4. The Medusa on Jeju Island, South Korea is

one of only twenty such instruments currently in operation globally and is uniquely sensitive

120   to the dominant emission sources of these compounds given its location in this highly

industrial part of the globe with large capacities of Al production, semiconductor

manufacturing, and rare earth element production industries. Its utility has already been

demonstrated in numerous previous studies to understand emissions of many GHGs from

Japan, South Korea, North Korea, eastern China, and surrounding countries (Fang et al.,

125   2015; Kim et al., 2010; Li et al., 2011).

For the first time we use the measurements of CF_4 (starting in 2008) and NF_3 (starting in

2013) in an inversion framework – coupling each measurement with an air history map

computed using a particle dispersion model. We demonstrate the use of these measurements to find emissions hotspots in this unique region with minimal use of prior information, and we show that East Asia is a major source of these species. Focussed mitigation efforts, based on these results, could have a significant impact on reducing GHG emissions from specific areas. The technology for abating emissions of these gases from such discrete sources exists and could be used (Chang and Chang, 2006; Purohit and Höglund-Isaksson, 2017; Illuzzi and Thewissen, 2010; Yang et al., 2009; Raoux, 2007; Wangxing et al., 2016).

2. Methods

2.1 Atmospheric measurements

The Gosan station (from here on termed GSN) is located on the south-western tip of Jeju Island in the Republic of Korea (126.16181° E, 33.29244° N). The station rests at the top of a 72 m cliff, about 100 km south of the Korean peninsula, 500 km northeast of Shanghai, China, and 250 km west of Kyushu, Japan, with an air inlet 17 m above ground level.

A Medusa GC-MS system was installed at GSN in 2007 and has been operated as part of the AGAGE network to take automated, high-precision measurements for a wide range of CFCs, HCFCs, HFCs, PFCs, Halons and other halocarbons; all significant synthetic GHG and/or stratospheric ozone depleting gases as well as many naturally occurring halogenated compounds (Miller et al., 2008; Arnold et al., 2012; Kim et al., 2010). Since November 2013, NF_3 has been measured within this suite of gases. Air reaches GSN from the most heavily developed areas of East Asia, making the measurements and their interpretation a unique source for 'top-down' emissions estimates in the region. Ambient air measurements are made every 130 minutes and are bracketed with a standard before and after the air sample in order to correct for instrumental drift in calibration. Further details on the methodology for the calibration of these gases are given elsewhere (Arnold et al., 2012; Mühle et al., 2010; Miller et al., 2010; Prinn et al., 2018).

2.2 Atmospheric model

Lagrangian particle dispersion models are well suited to determine emissions of trace gases on this spatial scale as they can be run backwards, allowing for the source-receptor relationship to be efficiently calculated. We use the Numerical Atmospheric dispersion Modelling Environment (NAME III), henceforth called NAME, developed by the UK Met Office (Ryall and Maryon, 1998; Jones et al., 2007). Inert particles are advected backwards in

160   time by the transport model, NAME, which also associates a mass to each trajectory. Hence, NAME output is provided as the time integrated near-surface (0 - 40 m) air concentration (g s m^{-3}) in each grid cell – the surface influence resulting from a conceptual release at a specific rate (g s^{-1}) from the site. 'Offline' this surface influence is divided by the total mass emitted during the 1-hour release time and multiplied by the geographical area of each grid box to

165   form a new array with each component representative of how 1 g m^{-2} s^{-1} of continuous emissions from a grid square would result in a measured concentration at the model's release point (the measurement site). Multiplication of each grid component by an emission rate then results in a contribution to the concentration.

The meteorological parameter inputs to NAME are from the Met Office's operational global

170   NWP model, the Unified Model (UM) (Cullen, 1993). The UM had a horizontal resolution of $0.5625° \times 0.375°$ ($\sim$40 km) from December 2007 to April 2010; $0.3516° \times 0.2344°$ ($\sim$25 km) from April 2010 to July 2014; and $0.234375 \times 0.15625°$ ($\sim$17 km) from mid-July 2014 to mid-July 2017. The number of vertical levels in the UM has increased over this period, with NAME taking the lowest 31 levels in 2009 and the lowest 59 levels in 2015. The GHGs

175   considered in this study have lifetimes on the order of hundreds to tens of thousands of years (Myhre et al., 2013), and can be considered inert gases on the spatial and temporal scales of this study and therefore the NAME model schemes for representing chemistry, dry deposition, wet deposition and radioactive decay were not used. The planetary boundary layer height (BLH) estimates are taken from the UM, however, a minimum BLH allowed

180   within NAME was set to 40 m to be consistent with the maximum emission height and the height of the output grid. The NAME model was run to estimate the 30-day history of the air on route to GSN. We calculated the time-integrated air concentration (dosage) at each grid box ($0.352° \times 0.234°$, and 0–40 m above ground level, irrespective of the underlying UM meteorology resolution) from a release of 1 g s^{-1} at GSN at 10±10 metres above the model

185   ground level (magl).

The model is three-dimensional, and therefore it is not just surface to surface transport that is modelled: An air parcel can travel from the surface to a high altitude and then back to the surface but only those times when the air parcel is within the lowest 40 m above the ground will it be included in the model output aggregated sensitivity maps. The computational

190   domain covers 54.34° E to 168.028° W longitude (391 grid cells of dimension 0.352°) and 5.3°S to 74.26°N latitude (340 grid cells of dimension 0.234°) and extends to more than 19 km vertically. Despite the increase in the resolution of the UM over the time period covered,

the resolution of the NAME output was kept constant throughout. For each 1 h period, 5000 inert model particles were used to describe the dispersion of air. By dividing the dosage [g s m^{-3}] by the total mass emitted [3600 s h^{-1} × 1 h × 1 g s^{-1}] and multiplying by the geographical area of each grid box [m^2], the model output was converted into a dilution matrix H [s m^{-1}]. In figure 1 we show an aggregated dilution matrix for the 2013 inversion period, demonstrating the areas of most significant influence on the GSN measurements. Each element of the matrix H dilutes a continuous emission of 1 g m^{-2} s^{-1} from a given grid box over the previous 30 d to simulate an average concentration [g m^{-3}] at the receptor (measurement point) during a 1 h period.

2.3 Inversion framework

For most long-lived trace gases (with lifetimes of years or longer), the assumption that atmospheric mole fractions respond linearly to changes in emissions holds well. By using this linearity, we can relate a vector of observations (y) to a state vector (x) made up of emissions and other non-prescribed model conditions (see section 2.6), via a sensitivity matrix (H) (Tarantola, 2005):

$$y = Hx + residual$$

A Bayesian framework is typically used in trace gas inversions and incorporates a priori information, which gives rise to the following cost function:

$$C = (Hx - y)^T R^{-1}(Hx - y) + (x - x_p)^T B^{-1}(x - x_p) \qquad (1)$$

Where, C is the cost function score (the aim is to minimise this score); H is made up mainly of the model derived dilution matrices (Section 2.2) but also the sensitivity of changes in domain border conditions on measured mixing ratios; x is a vector of emissions and domain border conditions; y is a vector of observations; R is a matrix of combined model and observation uncertainties; x_p is a vector of prior estimates of emissions and domain border conditions; and B is an error matrix associated with x_p. The cost function is minimised using a "NNLS", non-negative least squares fit (Lawson and Hanson, 1974), as previously used for volcanic ash (Thomson et al., 2017; Webster et al., 2017). The NNLS algorithm finds the least squares fit under the constraint that the emissions are non-negative. This is an "active set" method which efficiently iterates over choices for the set of emissions for which the non-negative constraint is active, i.e. the set of emissions which are set to zero.

The first term in equation 1 describes the mismatch (fit) between the modelled time-series and the observed time-series at each observation station. The observed concentrations (y) are comprised of two distinct components; (a) the Northern Hemisphere (NH) background concentration, referred to as the baseline, that changes only slowly over time, and (b) rapidly varying perturbations above the baseline. These observed deviations above background (baseline) are assumed to be caused by emissions on a regional scale that have yet to be fully mixed on the hemisphere scale. The magnitude of these deviations from baseline and, crucially, how they change as the air arriving at the stations travels over different areas, is the key to understanding where the emissions have occurred. The inversion system considers all of these changes in the magnitude of the deviations from baseline as it searches for the best match between the observations and the modelled time-series. The second term describes the mismatch (fit) between the estimated emissions and domain border conditions (x) and prior estimated emissions and domain border conditions (x_p) considering the associated uncertainties (B).

The aim of the inversion method is to estimate the spatial distribution of emissions across a defined geographical area. The emissions are assumed to be constant in time over the inversion time period (in this case one calendar year as is typically reported in inventories). Assuming the emissions are invariant over long periods of time is a simplification, but is necessary given the limited number of observations available. In order to compare the measurements and the model time-series, the latter are converted from air concentration [g m^{-3}] to the measured mole fraction (e.g. parts per trillion [ppt]) using the modelled temperature and pressure at the observation point.

2.4 Prior emissions information

Global emissions estimates of CF_4 and NF_3 using atmospheric measurements have demonstrated that 'bottom-up' accounting methods for one or more sectors, or one or more regions, are highly inaccurate (Arnold et al., 2013; Mühle et al., 2010). This study makes no effort to improve such inventory methods but instead focuses on minimising the reliance of prior information on our Bayesian-based posterior emissions estimates. Our prior information data sets come from the EDGAR (Emissions Database for Atmospheric Research) v4.2 emission grid maps (EC-JRC/PBL, 2013). This data set only covers the years 2000 to 2010 and therefore we apply the prior for 2010 for each year between 2011 and 2015. The 0.1 x 0.1° EDGAR emission maps were first re-gridded based on the lower resolution of our inversion grid (0.3516°× 0.2344°). In order to remove the influence of the within-country

prior spatial emissions distribution, each country's emissions were then averaged across their entire landmass (see Figure S1). We applied 5 different levels of uncertainty to each inversion grid cell (a,b) in 5 separate inversion experiments, each a multiple of the emissions magnitude ($x_{a,b}$) in each grid cell: $1 \times x_{a,b}$ (i.e. 100% uncertainty), $10 \times x_{a,b}$, $100 \times x_{a,b}$, $1000 \times x_{a,b}$, and $10,000 \times x_{a,b}$. We were then able to test the sensitivity of the prior emissions uncertainty and provide evidence for the low influence of prior information on the emissions estimates in the posterior.

2.5 Model-measurement and prior uncertainties

In addition to inaccurate prior information, another significant source of uncertainty in estimating emissions is from the model; from both the input meteorology and the atmospheric transport model itself. The uncertainty matrix, *R*, is a critical part of equation 1 that allows us to adjust uncertainties assigned to each measurement depending on how well we think the model is performing at that time: It describes, per hour time period, a combined uncertainty of the model and the observation at each time. The method of assigning measurement-model uncertainties is under development and here we describe one method that has been applied to the modelling of GSN measurements. All elements of the modelled meteorology (wind speed and direction, BLH, temperature, pressure, etc.) are important in understanding the dilution and uncertainty in modelling from source to receptor. However, quantifying the impact of each element that each model particle experiences in order to fully quantify the model uncertainty at each measurement time is beyond what is available from numerical weather prediction models. So in order to attempt to quantify a model/observation uncertainty we took a pragmatic approach and used modelled BHL at the receptor as a proxy.

Emissions are primarily diluted by transport and mixing within the planetary boundary layer (PBL), and hence, modelling of the PBL height (BLH) is crucial for accurate modelling of the mixing ratios. Changes in BLH at or surrounding the measurement location can cause significant changes to the measured mixing ratio. A low PBL (causing a larger model uncertainty) has two implications for measurements at the Gosan site: 1) A greater possibility of air from above the PBL being sampled in reality but not in the model. Subtle changes in the BLH at the exact measurement location are not well modelled and the difference between sampling above or within the PBL can have a significant influence on the amount of pollutant assigned to a back trajectory. 2) Greater influence of emissions from sources very near GSN. A lower BLH means that a lower rate of dilution of local emissions will occur, in turn increasing the signal of the local pollutant above the baseline. A relatively small change in a

290 low BLH will have a significant influence on this dilution compared to the same change on a high BLH. Thus, any error in the BHL at low levels can significantly amplify the uncertainty in the pollutant dilution. This is coupled with the fact that the modelled BLH has significant uncertainty especially when low.

To assign a model uncertainty to each hourly window of measurements we use model
295 information of BLH:

$$\sigma_{model} = \sigma_{baseline} \times f_{BLH}$$

where, $\sigma_{baseline}$ is the variability associated with the baseline calculation (see Section 2.6), and f_{BLH} is a multiplying factor (greater than or less than unity) that increases or decreases the relative uncertainty assigned to each model time period. f_{BLH} is based on modelled BLH
300 magnitude and variability over a three-hour period and is calculated with the following:

$$f_{BLH} = \frac{Max_{BLH-inlet}}{Min_{BLH-inlet}} \times \frac{Threshold}{Min_{BLH}}$$

where, $Max_{BLH-inlet}$ is the largest of either 100 m or the maximum distance, calculated hourly, between the inlet and the modelled BLH within a period of three hours around the measurement time; $Min_{BLH-inlet}$ is the smallest of the distances calculated between the inlet
305 and the BLH over the same three-hour period; $Threshold$ is an arbitrary value set at 500 m; and Min_{BLH} is the lowest BLH recorded over the three-hour period. Thus, the relative assigned uncertainty considers the proximity of the varying BLH to the inlet height and a recognition that observations taken when the BLH is varying at higher altitudes (>500 m a.g.l.) is likely to have less impact and therefore have lower uncertainty compared to those
310 taken when the BLH is varying at lower altitudes (< 500 magl).

Supporting Figures S2-S6 show annual time series of observations and the corresponding measurement-model uncertainties, as well as statistics for the mismatch between observations and modelled time series.

2.6 Baseline calculation and domain border conditions

315 For each measurement at GSN it is important to accurately understand the portion of the total mixing ratio arriving from outside the inversion domain and the portion from emission sources within the domain, otherwise emissions from specific areas could be over or under estimated. GSN is uniquely situated; receiving air masses from all directions over the course

of the year, which can have distinct compositions of trace gases, driven mainly by the
320   different emission rates between the two hemispheres and slow inter-hemispheric mixing.

In addition to the time integrated air concentration produced by NAME (Section 2.2), the 3D coordinate where each particle left the computational domain was also recorded. This information was then post-processed to produce the percentage contributions from 11 different borders of the 3D domain (Figure 2). From 0 to 6 km in height eight horizontal
325   boundaries (WSW, WNW, NNW, NNE, ENE, ESE, SSE, SSW) were considered and between 6 to 9 km the horizontal boundaries were only split between north and south. The eleventh border was considered when particles left in any direction above 9 km. Thus, the influence of air arriving to GSN from outside the domain was simplified as a combination of air masses arriving from 11 discrete directions.

330   We use measurements from the Mace Head observatory (from here termed MHD) on the west coast of Ireland (53.33° N, 9.90° W) – a key AGAGE (Advanced Global Atmospheric Gases Experiment) site providing long term in-situ atmospheric measurements – to act as a starting point for an estimate of the composition of air from the NH mid-latitudes entering the East Asia domain. MHD was one of the first locations to measure CF_4 (starting 2004) and
335   NF_3 (starting 2012) and other measurements from the site are routinely used in atmospheric studies to calculate decadal trends in the NH atmospheric abundances. In summary, a quadratic fit was made only to MHD observations that were representative of the NH baseline. i.e. when well mixed air was arriving predominately from the WNW-NNW (North Atlantic) direction as calculated using NAME (details of filtering and fitting are given in the
340   Supporting Text).

The composition of air arriving from any of the 11 directions is calculated using corresponding multiplying factors applied to the MHD baseline, which were included as part of the state vector (x), i.e. these factors are constant for a given inversion year. The prior baseline was therefore perturbed as part of the inversion based on the relative contribution of
345   air arriving from different borders of the 3D domain and the multiplying factors that are included within the cost function (Equation 1). Figure 3 shows an annual time series of observations for CF_4 and the difference between the prior baseline (the quadratic fit from MHD) and the posterior baseline.

2.7 Domains and inversion grids

350 The domain used in the inversion is smaller than the computational NAME transport model domain. The horizontal inversion domain covers 88.132° E to 145.860° E longitude (164 fine grid cells of 0.352°) and 15.994° N to 57.646° N latitude (178 fine grid cells of 0.234°). GSN is within a region surrounded by countries with major developed industries and therefore the site is relatively insensitive to emissions from further away that are diluted on route to the

355 site. NAME is run on a larger domain to ensure that on the occasion when air circulates out of the inversion domain and then back, its full 30-day history in the inversion domain is included.

An initial computational inversion grid (from here termed the 'coarse grid') was created based on a) aggregated information from the NAME footprints over the period of the

360 inversion (in this case one year), aggregating fewer grid cells in areas that are 'seen' the most by GSN, and b) on the prior emissions flux i.e. areas known to have low emissions (e.g. ocean) had higher aggregation. Coarse grid cells could not be aggregated over more than a single country/region and a total of ≈100 coarse grid cells (n) were created. After the initial inversion a coarse grid cell was chosen to divide in two by area. The decision on which single

365 coarse grid cell to split is calculated based on the posterior emissions density [g yr^{-1} m^{-2}] of the coarse grids and the ability of the posterior emissions to impact the measurements at GSN (using information from the NAME output). A new inversion was run using identical inputs except for the number of grid cells (now n+1). This sequence was repeated 50 times creating ≈150 coarse grid cells within the inversion domain for the final inversion. The results from

370 the inversions with the maximum disaggregation are presented in this paper.

3. Results and discussion

3.1 Country total emissions estimates

Table 1 provides a summary of our estimates of emissions from the five major emitting countries/regions within the East Asia domain. These posterior emission estimates use a prior

375 emissions uncertainty in each fine grid cell of 100x the emissions magnitude (see Section 2.4).

HFC-23

Fang et al. (2015) conducted a very thorough 'bottom-up' study within their work on HFC-23; constraining an inversion model using both prior information and atmospheric

380 measurements. They used an inverse method based on FLEXPART using measurements from three sites in East Asia – GSN, Hateruma (a Japanese island ~200 km east of Taiwan),

and Cape Ochi-ishi (northern Japan), calculating an HFC-23 emissions rise in China from 6.4 $\pm$ 0.7 Gg yr^{-1} in 2007 (6.2 $\pm$ 0.6 Gg yr^{-1} in 2008) to 8.8 $\pm$ 0.8 Gg yr^{-1} in 2012. An earlier study by Stohl et al. (2010) also report HFC-23 emissions of 6.2 $\pm$ 0.8 Gg yr^{-1} in 2008. Both Fang et al. (2015) and Stohl et al. (2010) report emissions from other countries below 0.25 Gg yr^{-1} for all years. Our estimates use a completely independent inverse method and only data from GSN, yet the results are very close to those of Fang et al. (2015) (Figure 4): 6.8 $\pm$ 4.3 Gg yr^{-1} in 2008 (a difference of 10%) and 10.7 $\pm$ 4.6 Gg yr^{-1} in 2012 (a difference of 22%), and of Stohl et al. (2010). The posterior uncertainties in these two different studies mainly reflect the difference in the prior uncertainty assumed for the prior information: We assume a very high level of uncertainty on our prior emissions and therefore our posterior uncertainties are significantly higher. However, these inversion result estimates are lower than estimates based on inter-species correlation analysis by Li et al. (2011) who calculated emissions of HFC-23 from China in 2008 in the range of 7.2-13 Gg yr^{-1}. And using a CO tracer-ratio method, Yao et al. (2012) estimated particularly low emissions of 2.1 $\pm$ 4.6 Gg yr^{-1} for 2011-2012. The estimates derived from atmospheric inversions do not rely on any correlations with other species or known emissions for certain species, and given two separate inversion studies have produced very similar results we suggest these provide a more reliable 'top-down' emissions estimate of HFC-23. As well as providing an independent validation of the previous work on HFC-23 by Fang et al. (2015) and Stohl et al. (2010), the alignment of our HFC-23 emissions estimates with those previous studies provides confidence in our inversion methodology for the CF_4 and NF_3 emissions estimates.

CF_4

Our understanding of emissions of CF_4 and NF_3 is very poor, which is highlighted in global studies based on atmospheric measurements that show bottom-up estimates of emissions are significantly underestimated (Mühle et al., 2010; Arnold et al., 2013). With such a poor prior understanding of emissions we assess the effect of prior uncertainty on the posterior emissions (Figure 4). With assignment of uncertainty on the prior of each fine grid cell at ten times the prior emissions value, the posterior is still significantly constrained by the prior for both China and South Korea. When larger uncertainties are applied to the prior (100x to 10000x) the posterior estimates are very consistent, indicating that when greater than 100x uncertainty is applied, emissions estimates are most significantly constrained by the atmospheric measurements. For China for 7 of the 8 years studied our posterior estimates are greater than twice the prior estimates taken from EDGAR v4.2. The latest global estimates

415   are from Rigby et al. (2014) and they estimated global CF_4 emissions of 10.4 ± 0.6 Gg/year in

2008 with a steady but small increase to 11.1 ± 0.4 Gg/year in 2013 (with the exception of a

dip in 2009 to 9.3 ± 0.5 Gg/year). We highlight that our Chinese emission estimates remain

within a narrow range for 5 of the 8 years studied at between 4.0 and 4.7 Gg/year (with

typical uncertainties <2.7 Gg/year), and for 7 of the 8 years studied between 2.82 and 5.35

420   Gg/year. However, the estimate for 2012 appears to be anomalous at 8.25 ± 2.59 Gg/year. In

relation to the global top-down estimates from 2008 to 2012, our Chinese estimates represent

between 37 to 45 % of global emissions between 2008 and 2011 with a jump to 74 % in

2012. This significant increase in 2012 is not reconcilable with atmospheric measurements on

the global scale and is very likely a spurious result of the inversion. The most probable

425   explanation for such a result is the incorrect assignment of emissions on the inversion grid.

Incorrect assignment of emissions can occur between countries, particularly where air parcels

frequently pass over more than one country, therefore reducing the ability of the inversion to

confidently place emissions. However, there is not an obvious drop in emissions for another

country in 2012 that would offset the large increase in the Chinese emissions estimate.

430   Within a country, incorrect assignment of emissions from an area closer to the receptor to an

area further from the receptor will increase the calculated total emissions owing to increased

dilution in going from a near to a far source. Our inversion is susceptible to this effect as we

only have one site for assimilation of measurements; two measurement sites, spaced apart

and straddling the area of interest, would provide significantly more information to constrain

435   the spatial emissions distribution.

Our estimates are significantly higher than emission estimation methods using interspecies

correlation: Kim et al. (2010) estimated CF_4 emissions in the range of only 1.7-3.1 Gg yr^{-1} in

2008 and Li et al. (2011) only 1.4-2.9 Gg yr^{-1} over the same period. The interspecies

440   correlation approach inherently requires that the sources of the different gases that are

compared are coincident in time and space. Kim et al. (2010) and Li et al. (2011) used

HCFC-22 as the tracer compound for China with a calculated emissions field from an inverse

model and most emissions of this gas originate from fugitive release from air conditioners

and refrigerators. However, CF_4 is emitted mostly from point sources in the semiconductor

445   and aluminium production industries with different spatial emissions distribution within

countries, and likely different temporal characteristics compared to HCFC-22.

Emissions estimates from South Korea and Japan are one order of magnitude lower than for China. For 2008 Li et al. (2011) estimate emissions of CF_4 from combined South and North Korea of 0.19-0.26 Gg yr^{-1} and from Japan of 0.2-0.3 Gg yr^{-1}, which are on the low end of the uncertainty range of our estimates for that year (Table 1). As one of the largest, if not the largest, country for semiconductor wafer production, Taiwan is also an emitter of CF_4. However, measurements at GSN provide only poor sensitivity to detection of emissions from Taiwan and our results can only suggest that emissions are likely <0.5 Gg yr^{-1}. North Korea emissions were small and no annual estimate was above 0.1 Gg yr^{-1}.

NF$_3$

Our understanding of NF_3 emissions from inventory and industry data is even poorer than for CF_4. On a global scale the emission estimates from industry are underestimated (Arnold et al., 2013). This study suggests that at least some emissions of NF_3 stem from China, however gaining meaningful quantitative estimates has been difficult due to large uncertainties (Figure 4). Contrastingly, the posterior estimates of emissions from South Korea have relatively small uncertainties. Emissions from China travel a greater distance to the measurement site compared to emissions from South Korea. Thus, the magnitudes of NF_3 pollution events from China (especially from provinces furthest west), in terms of the mixing ratio detected at GSN, are smaller than for pollution arriving from neighbouring South Korea. Also, the poorer measurement precision for NF_3 compared to CF_4 leads to a larger uncertainty on the baseline, which in turn affects the certainty on the pollution episode, especially for more dilute signals. Emissions estimates for Japan are difficult to make without improved prior information and more atmospheric measurements in other locations. We argue that other large changes in our emissions estimates from 2014 to 2015 could be real. For example, Japan's National Inventory Report for NF_3 shows a reduction in emissions of 63% between 2013 and 2015 (Ministry of the Environment Japan et al., 2018), which is within the uncertainty of the relative rate of decrease we observe.

As for CF_4, emission estimates of NF_3 from Taiwan and North Korea are highly uncertain. However, our results do indicate that emissions of NF_3 from Taiwan might be lower than from South Korea despite very similar sized semiconductor production industries. Focussing on the more meaningful estimates from South Korea, emissions of NF_3 in 2015 are estimated to be 0.60 ± 0.07 Gg yr^{-1} which equates to 9660 ± 1127 Gg yr^{-1} CO_2-equivalent emissions (based on a GWP$_{100}$ of 16,100). This is ~1.6% of the country's CO_2 emissions (Olivier et al., 2017), thus making a significant impact on their total GHG budget. Further, given that the

480   sources of NF_3 are relatively few, these emissions can be assigned to a small number of

industries, potentially making NF_3 an easy target for focussed mitigation policy. Rigby et al.

(2014a) updated the global emission estimates from Arnold et al. (2013), and calculated an

annual emissions estimate of 1.61 Gg yr^{-1} for 2012, with an average annual growth rate over

the previous 5 years of 0.18 Gg yr^{-1}. Linearly extrapolating this growth to 2014 and 2015

485   leads to projected global emissions of 1.97 and 2.15 Gg yr^{-1} for 2014 and 2015, respectively.

Thus, South Korean emissions as a percentage of these global totals equate to ~20% and

~28% for 2014 and 2015, respectively, which is around the proportion of semiconductor

wafer fabrication capacity in South Korea relative to global totals (~20%) (SEMI, 2017).

490   **3.2 Spatial emission maps**

We use 'emissions minus uncertainty' maps (e.g. Figure 5B) is to provide information on

where we are most certain of large emissions i.e. where emission hotpots are located and if

they are significant: Less negative values indicate more certainty, with positive values

indicating that the uncertainty is less than the best estimate and negative values indicating

495   that the uncertainty is bigger than the estimate. A more common way to illustrate grid-level

uncertainty is in an 'uncertainty reduction' map. This works well when starting from a

relatively well-constrained, spatially resolved prior to illustrate the additional constraint the

atmospheric observations add. In this study, however, we are starting from very poor prior

information and we generate a posterior emission map that is very distinct from the prior,

500   informed largely by the measurements. Thus, an uncertainty reduction map provides little

useful information.

Figure 5 shows the effect of re-gridding over the course of 50 separate CF_4 inversions (for

2015), from zero re-gridding steps (i.e. using a coarse grid space determined using

information from NAME and the prior emissions), through to 25, and then 50 steps. The

505   inversion was not allowed to decrease the minimum posterior grid size beyond four fine grid

squares (i.e. four times the $0.3516° \times 0.2344°$ grid square). This method highlights the areas

that have the highest emissions density; the splitting of these grid cells improves the

correlation between observations and posterior model output. However, these emission maps

must be studied alongside the corresponding uncertainty maps. The inversion could continue

510   to split towards a fine grid resolution limit even though there may not be enough information

in the data to accurately constrain emissions from each course grid cell (leading to spurious

emission patterns) and the process would be computationally very expensive. The largest emissions of CF_4 arise from China and Figure 5 suggests the largest emissions come from an area between 35° N and 38° N. The uncertainty on these emissions from the specific final

515   coarse grid squares is large (Figure 5F) and therefore care needs to be taken not to over interpret emission hotspots. Although the grid is being split it is not realistic for the model to correctly interpret the spatial distribution of emissions at this distance from GSN, and this is demonstrated in Figure 5F where the relative error on emissions in this corner of the domain is large. Without better prior information it is not possible to distinguish between real year-to-

520   year emission pattern changes and inaccurate emission patterns (Figure 6 and S7). Over the period of study emissions of CF_4 generally appear to arise from north of 30° N and in 2008 and 2013 emissions appear around 25° N. However, GSN does not have good sensitivity to emissions from this area and it is possible that these emissions could be incorrectly assigned from Taiwan. Although emissions from South Korea are significantly lower than for China,

525   the proximity to GSN causes the grid cells to be split and emissions to be assigned at higher spatial resolution, and generally (except for 2008) in the north-west quadrant of the country. Splitting of grid cells in South Korea decreased the relative error on the emissions from particular grid squares, providing confidence that the placement of emissions is accurate. Further, for sequential years 2013, 2014 and 2015 two specific grid cells in that north-west

530   quadrant are highlighted with comparatively low uncertainties (Figure S7). How well these consistent year-to-year emission patterns in South Korea correlate with the actual location of emissions needs to be the subject of further study (e.g. improved bottom-up inventory compilation efforts). Emissions from Japan are too uncertain to explore the spatial emissions pattern.

535   For NF_3, emissions from China and Japan are too low and uncertain to interpret at finer spatial resolution. However, as with CF_4, it is interesting to study the relatively more certain spatially disaggregated emissions from South Korea (Figure 7). In common with CF_4, NF_3 emissions from the south-west area are minimal, however in contrast to CF_4, emissions occur on the eastern side of South Korea and on the south east coast. Emissions from the south east

540   coast coincide with the known location of a production plant for NF_3 located in the area of Ulsan (Gas World, 2011). If this plant is sufficiently separated in space from the end-users of NF_3 then this result would indicate that production of NF_3, not just use, could be a significant source in South Korea.

The study of Fang et al. (2015) highlights three major hotspots for HFC-23 emissions in China based on HCFC-22 production facility locations. Our posterior maps (Figure 8) correctly show the bulk of emissions in far eastern China, in line with the results of Fang et al. (2015). However, given the inconsistency of emissions maps between years we are unable to provide any more information without a better spatially disaggregated prior emissions map.

Conclusions

We largely remove the influence of 'bottom-up' information and present the first Bayesian inversion estimates of CF_4 and NF_3 from the East Asia region using measurements from a single atmospheric monitoring site, GSN station located on the island of Jeju (South Korea). The largest CF_4 emissions are from China, estimated at 4-6 Gg yr^{-1} for six out of the eight years studied, which is significantly larger than previous estimates. Despite significantly smaller emissions from South Korea, the spatial disaggregation of CF_4 emissions were consistent between independent inversions based on annual measurement data sets, indicating the north west of South Korea is a hotspot for significant CF_4 release, presumably from the semiconductor industry. Emissions of NF_3 from South Korea were quantifiable with significant certainty, and represent large emissions on a CO_2-equivalent basis (~1.6% of South Korea's CO_2 emissions in 2015). HFC-23 emissions were also calculated using the same inversion methodology with high uncertainty on prior information. We found good agreement with other studies in terms of aggregated country totals and spatial emissions patterns, providing confidence that our methodology is suitable and conclusions justified for estimates of CF_4 and NF_3.

Our results highlight an inadequacy in both the bottom-up reported estimates for CF_4 and NF_3 and the limitations of the current measurement infrastructure for 'top-down' estimates for these specific gases. Adequate bottom-up estimates have been lacking, owing to the absence of reporting requirements for these gases from China and South Korea, and top-down estimates have been hampered by poor measurement coverage owing to the technical complexities required to measure these volatile, low abundance gases at high precision. Improvements in both bottom-up information and measurement coverage, alongside refinements in transport modelling and developments in inversion methodologies, will lead to improved optimal emissions estimates of these gases in future studies.

Acknowledgements

Observations at GSN were supported by the Basic Science Research Program through the
National Research Foundation of Korea (NRF) funded by the Ministry of Education (No. NRF-2016R1A2B2010663). The UK's Department for Business, Energy & Industrial Strategy (BEIS) funded the MHD measurements and the development of InTEM.

References

Arnold, T., Mühle, J., Salameh, P. K., Harth, C. M., Ivy, D. J., and Weiss, R. F.: Automated measurement of nitrogen trifluoride in ambient air, Anal. Chem., 84, 4798–4804, 10.1021/ac300373e, 2012.

Arnold, T., Harth, C., Mühle, J., Manning, A. J., Salameh, P., Kim, J., Ivy, D. J., Steele, L. P., Petrenko, V. V., Severinghaus, J. P., Baggenstos, D., and Weiss, R. F.: Nitrogen trifluoride global emissions estimated from updated atmospheric measurements, Proceedings of the National Academy of Sciences, 110, 2019–2034, 2013.

Bronfin, B. R., and Hazlett, R. N.: Synthesis of nitrogen fluorides in a plasma jet, Industrial & Engineering Chemistry Fundamentals, 5, 472-478, 10.1021/i160020a007, 1966.

Chang, M. B., and Chang, J.-S.: Abatement of PFCs from Semiconductor Manufacturing Processes by Nonthermal Plasma Technologies: A Critical Review, Industrial & Engineering Chemistry Research, 45, 4101-4109, 10.1021/ie051227b, 2006.

Cullen, M. J. P.: The unified forecast/climate model, Meteorological Magazine, 122, 81-94, 1993.

Deeds, D. A., Vollmer, M. K., Kulongoski, J. T., Miller, B. R., Muhle, J., Harth, C. M., Izbicki, J. A., Hilton, D. R., and Weiss, R. F.: Evidence for crustal degassing of CF4 and SF6 in Mojave Desert groundwaters, Geochimica et Cosmochimica Acta, 72, 999-1013, 10.1016/j.gca.2007.11.027, 2008.

EC-JRC/PBL: Emission Database for Global Atmospheric Research (EDGAR), release version 4.2. In: http://edgar.jrc.ec.europa.eu/, Source: European Commission, Joint Research Centre (JRC)/Netherlands Environmental Assessment Agency (PBL), 2013.

Fang, X., Miller, B. R., Su, S., Wu, J., Zhang, J., and Hu, J.: Historical Emissions of HFC-23 (CHF3) in China and Projections upon Policy Options by 2050, Environ. Sci. Technol., 48, 4056-4062, 10.1021/es404995f, 2014.

Fang, X., Stohl, A., Yokouchi, Y., Kim, J., Li, S., Saito, T., Park, S., and Hu, J.: Multiannual Top-Down Estimate of HFC-23 Emissions in East Asia, Environ. Sci. Technol., 49, 4345-4353, 10.1021/es505669j, 2015.

Gas World: Air Products doubles NF3 facility at Ulsan, Korea. 2011.

Henderson, P. B., and Woytek, A. J.: Nitrogen–nitrogen trifluoride, in: Kirk–Othmer Encyclopedia of Chemical Technology, 4th ed., edited by: Kroschwitz, J. I., and Howe-Grant, M., John Wiley & Sons, New York, 1994.

Illuzzi, F., and Thewissen, H.: Perfluorocompounds emission reduction by the semiconductor industry, Journal of Integrative Environmental Sciences, 7, 201-210, 10.1080/19438151003621417, 2010.

620 International Aluminium Institute: The International Aluminium Institute Report on the Aluminium Industry's Global Perfluorocarbon Gas Emissions Reduction Programme – Results of the 2015 Anode Effect Survey, International Aluminum Institute, London, 1–56, 2016.

International SEMATECH Manufacturing Initiative: Reduction of Perfluorocompound (PFC) Emissions: 2005 State of the Technology Report, International SEMATECH Manufacturing
625 Initiative, 2005.

Johnson, A. D., Entley, W. R., and Maroulis, P. J.: Reducing PFC gas emissions from CVD chamber cleaning, Solid State Technology, 43, 103-114, 2000.

Jones, A., Thomson, D., Hort, M., and Devenish, B.: The UK Met Office's next-generation atmospheric dispersion model, NAME III, Air Pollution Modeling and Its Applications Xvii,
630 edited by: Borrego, C., and Norman, A. L., 580-589 pp., 2007.

Keller, C. A., Hill, M., Vollmer, M. K., Henne, S., Brunner, D., Reimann, S., O'Doherty, S., Arduini, J., Maione, M., Ferenczi, Z., Haszpra, L., Manning, A. J., and Peter, T.: European Emissions of Halogenated Greenhouse Gases Inferred from Atmospheric Measurements, Environ. Sci. Technol., 46, 217-225, 10.1021/es202453j, 2012.

635 Kim, J., Li, S., Kim, K. R., Stohl, A., Mühle, J., Kim, S. K., Park, M. K., Kang, D. J., Lee, G., Harth, C. M., Salameh, P. K., and Weiss, R. F.: Regional atmospheric emissions determined from measurements at Jeju Island, Korea: Halogenated compounds from China, Geophys. Res. Lett., 37, L12801 10.1029/2010gl043263, 2010.

640 Kim, J., Fraser, P. J., Li, S., Muhle, J., Ganesan, A. L., Krummel, P. B., Steele, L. P., Park, S., Kim, S. K., Park, M. K., Arnold, T., Harth, C. M., Salameh, P. K., Prinn, R. G., Weiss, R. F., and Kim, K. R.: Quantifying aluminum and semiconductor industry perfluorocarbon emissions from atmospheric measurements, Geophys. Res. Lett., 41, 4787-4794, 10.1002/2014gl059783, 2014.

645 Lawson, C. L., and Hanson, R. J.: Solving Least Squares Problems, Classics in Applied Mathematics, 1974.

Li, S., Kim, J., Kim, K.-R., Muehle, J., Kim, S.-K., Park, M.-K., Stohl, A., Kang, D.-J., Arnold, T., Harth, C. M., Salameh, P. K., and Weiss, R. F.: Emissions of Halogenated Compounds in East Asia Determined from Measurements at Jeju Island, Korea, Environ. Sci.
650 Technol., 45, 5668-5675, 10.1021/es104124k, 2011.

McCulloch, A., and Lindley, A. A.: Global emissions of HFC-23 estimated to year 2015, Atmos. Environ., 41, 1560-1566, 10.1016/j.atmosenv.2006.02.021, 2007.

Miller, B. R., Weiss, R. F., Salameh, P. K., Tanhua, T., Greally, B. R., Mühle, J., and Simmonds, P. G.: Medusa: A sample preconcentration and GC/MS detector system for in situ
655 measurements of atmospheric trace halocarbons, hydrocarbons, and sulfur compounds, Anal. Chem., 80, 1536–1545, 10.1021/ac702084k, 2008.

Miller, B. R., Rigby, M., Kuijpers, L. J. M., Krummel, P. B., Steele, L. P., Leist, M., Fraser, P. J., McCulloch, A., Harth, C., Salameh, P., Mühle, J., Weiss, R. F., Prinn, R. G., Wang, R. H. J., O'Doherty, S., Greally, B. R., and Simmonds, P. G.: HFC-23 (CHF_3) emission trend response to HCFC-22 ($CHClF_2$) production and recent HFC-23 emission abatement measures, Atmos. Chem. Phys., 10, 7875–7890, 10.5194/acp-10-7875-2010, 2010.

Ministry of the Environment Japan, Greenhouse Gas Inventory Office of Japan, Center for Global Environmental Research, and National Institute for Environmental Studies, J.: National Greenhouse Gas Inventory Report of JAPAN, 2018.

Montzka, S. A., Kuijpers, L., Battle, M. O., Aydin, M., Verhulst, K. R., Saltzman, E. S., and Fahey, D. W.: Recent increases in global HFC-23 emissions, Geophys. Res. Lett., 37, 10.1029/2009gl041195, 2010.

Mühle, J., Ganesan, A. L., Miller, B. R., Salameh, P. K., Harth, C. M., Greally, B. R., Rigby, M., Porter, L. W., Steele, L. P., Trudinger, C. M., Krummel, P. B., O'Doherty, S., Fraser, P. J., Simmonds, P. G., Prinn, R. G., and Weiss, R. F.: Perfluorocarbons in the global atmosphere: tetrafluoromethane, hexafluoroethane, and octafluoropropane, Atmos. Chem. Phys., 10, 5145–5164, 10.5194/acp-10-5145-2010, 2010.

Myhre, G., Shindell, D., Bréon, F.-M., Collins, W., Fuglestvedt, J., Huang, J., Koch, D., Lamarque, J.-F., Lee, D., Mendoza, B., Nakajima, T., Robock, A., Stephens, G., Takemura, T., and Zhang, H.: Anthropogenic and Natural Radiative Forcing, in: Climate Change 2013: The Physical Science Basis. Contribution of Working Group I to the Fifth Assessment Report of the Intergovernmental Panel on Climate Change, edited by: Stocker, T. F., Qin, D., Plattner, G.-K., Tignor, M., Allen, S. K., Boschung, J., Nauels, A., Xia, Y., Bex, V., and Midgley, P. M., Cambridge University Press, Cambridge, United Kingdom and New York, NY, USA, 659–740, 2013.

Olivier, J. G. J., Schure, K. M., and Peters, J. A. H. W.: Trends in global CO2 emissions; 2017 Report, PBL Netherlands Environmental Assessment Agency, The Hague/Bilthoven500114022, 2017.

Prinn, R. G., Weiss, R. F., Arduini, J., Arnold, T., DeWitt, H. L., Fraser, P. J., Ganesan, A. L., Gasore, J., Harth, C. M., Hermansen, O., Kim, J., Krummel, P. B., Li, S., Loh, Z. M., Lunder, C. R., Maione, M., Manning, A. J., Miller, B. R., Mitrevski, B., Mühle, J., O'Doherty, S., Park, S., Reimann, S., Rigby, M., Saito, T., Salameh, P. K., Schmidt, R., Simmonds, P. G., Steele, L. P., Vollmer, M. K., Wang, R. H., Yao, B., Yokouchi, Y., Young, D., and Zhou, L.: History of Chemically and Radiatively Important Atmospheric Gases from the Advanced Global Atmospheric Gases Experiment (AGAGE), Earth Syst. Sci. Data Discuss., 1-39, 10.5194/essd-2017-134, 2018.

Purohit, P., and Höglund-Isaksson, L.: Global emissions of fluorinated greenhouse gases 2005–2050 with abatement potentials and costs, Atmos. Chem. Phys., 17, 2795-2816, 10.5194/acp-17-2795-2017, 2017.

Raoux, S.: Implementing technologies for reducing PFC emissions, Solid State Technology, 50, 49-52, 2007.

Rigby, M., Prinn, R. G., O'Doherty, S., Miller, B. R., Ivy, D., Muhle, J., Harth, C. M., Salameh, P. K., Arnold, T., Weiss, R. F., Krummel, P. B., Steele, L. P., Fraser, P. J., Young,

D., and Simmonds, P. G.: Recent and future trends in synthetic greenhouse gas radiative
700 forcing, Geophys. Res. Lett., 41, 2623-2630, 10.1002/2013gl059099, 2014a.

Rigby, M., Prinn, R. G., O'Doherty, S., Miller, B. R., Ivy, D., Mühle, J., Harth, C. M.,
Salameh, P. K., Arnold, T., Weiss, R. F., Krummel, P. B., Steele, L. P., Fraser, P. J., Young,
D., and Simmonds, P. G.: Recent and future trends in synthetic greenhouse gas radiative
forcing, Geophys. Res. Lett., 41, 2623-2630, 10.1002/2013gl059099, 2014b.

705 Ryall, D. B., and Maryon, R. H.: Validation of the UK Met. Office's name model against the
ETEX dataset, Atmos. Environ., 32, 4265-4276, 10.1016/s1352-2310(98)00177-0, 1998.

SEMI: SEMI® World Fab Forecast. SEMI (Ed.),
http://www.semi.org/en/Store/MarketInformation/fabdatabase/ctr_027238, 2017.

Simmonds, P. G., Rigby, M., McCulloch, A., Vollmer, M. K., Henne, S., Mühle, J.,
710 O'Doherty, S., Manning, A. J., Krummel, P. B., Fraser, P. J., Young, D., Weiss, R. F.,
Salameh, P. K., Harth, C. M., Reimann, S., Trudinger, C. M., Steele, L. P., Wang, R. H. J.,
Ivy, D. J., Prinn, R. G., Mitrevski, B., and Etheridge, D. M.: Recent increases in the
atmospheric growth rate and emissions of HFC-23 (CHF3) and the link to HCFC-22
(CHClF2) production, Atmos. Chem. Phys., 18, 4153-4169, 10.5194/acp-18-4153-2018,
715 2018.

Stohl, A., Kim, J., Li, S., O'Doherty, S., Mühle, J., Salameh, P. K., Saito, T., Vollmer, M. K.,
Wan, D., Weiss, R. F., Yao, B., Yokouchi, Y., and Zhou, L. X.: Hydrochlorofluorocarbon
and hydrofluorocarbon emissions in East Asia determined by inverse modeling, Atmos.
Chem. Phys., 10, 3545-3560, 2010.

720 Thomson, D. J., Webster, H. N., and Cooke, M. C.: Developments in the Met Office InTEM
volcanic ash source estimation system, Part 1: Concepts Met Office, 2017.

Totterdill, A., Kovács, T., Feng, W., Dhomse, S., Smith, C. J., Gómez-Martín, J. C.,
Chipperfield, M. P., Forster, P. M., and Plane, J. M. C.: Atmospheric lifetimes, infrared
absorption spectra, radiative forcings and global warming potentials of NF3 and
725 CF3CF2Cl (CFC-115), Atmos. Chem. Phys., 16, 11451-11463, 10.5194/acp-16-11451-2016,
2016.

Vogel, H., Flerus, B., Stoffner, F., and Friedrich, B.: Reducing Greenhouse Gas Emission
from the Neodymium Oxide Electrolysis. Part I: Analysis of the Anodic Gas Formation,
Journal of Sustainable Metallurgy, 3, 99-107, 10.1007/s40831-016-0086-0, 2017.

730 Wangxing, L., Xiping, C., Shilin, Q., Baowei, Z., and Bayliss, C.: Reduction Strategies for
PFC Emissions from Chinese Smelters, in: Light Metals 2013, edited by: Sadler, B. A.,
Springer International Publishing, Cham, 893-898, 2016.

Webster, H. N., Thomson, D. J., and Cooke, M. C.: Developments in the Met Office
InTEMvolcanic ash source estimation system, Part 2: Results, Met Office, 2017.

735 World Semiconductor Council: Joint Statement of the 21st Meeting of the World
Semiconductor Council (WSC). Kyoto, Japan, 2017.

Yang, C.-F. O., Kam, S.-H., Liu, C.-H., Tzou, J., and Wang, J.-L.: Assessment of removal efficiency of perfluorocompounds (PFCs) in a semiconductor fabrication plant by gas chromatography, Chemosphere, 76, 1273-1277, 10.1016/j.chemosphere.2009.06.039, 2009.

740 Yao, B., Vollmer, M. K., Zhou, L. X., Henne, S., Reimann, S., Li, P. C., Wenger, A., and Hill, M.: In-situ measurements of atmospheric hydrofluorocarbons (HFCs) and perfluorocarbons (PFCs) at the Shangdianzi regional background station, China, Atmos. Chem. Phys., 12, 10181-10193, 10.5194/acp-12-10181-2012, 2012.

Yokouchi, Y., Taguchi, S., Saito, T., Tohjima, Y., Tanimoto, H., and Mukai, H.: High 745 frequency measurements of HFCs at a remote site in east Asia and their implications for Chinese emissions, Geophys. Res. Lett., 33, n/a-n/a, 10.1029/2006GL026403, 2006.

Zhang, L., Wang, X., and Gong, B.: Perfluorocarbon emissions from electrolytic reduction of rare earth metals in fluoride/oxide system, Atmospheric Pollution Research, doi:10.1016/j.apr.2017.06.006., 2017.
750

Figures

Figure 1: An aggregation of the dilution matrices from 2013, generated using NAME output (see section 2.2), illustrating the relative sensitivity of measurements at GSN to emissions in the region.

Figure 2: Schematic of the domain borders as applied in the inversion. 11 domain border conditions were estimated as depicted from 1 to 11 as a multiplying factor to the prior baseline estimated using data from the Mace Head observatory. Below 6 km the domain border was divided 8 times: NNE, ENE, ESE, SSE, SSW, WSW, WNW and NNW; between 6 to 9 km the domain border was just divided between north and south; and air arriving from above 9 km was considered from one 'high' domain border. Average posterior multiplying factors for CF_4 over the eight years were 1.00 ± 0.01 (NNE), 0.97 ± 0.06 (ENE), 1.02 ± 0.05 (ESE), 0.99 ± 0.01 (SSE), 1.00 ± 0.01 (SSW), 0.99 ± 0.01 (WSW), 1.00 ± 0.00 (WNW), 1.00 ± 0.01 (NNW), 1.00 ± 0.00 (6 to 9 km north), 1.00 ± 0.05 (6 to 9 km south), 0.97 ± 0.03 (above 9 km).

Figure 3: Time series of CF_4 measurements during 2013 – an example year with the most uninterrupted time series. Prior baseline (blue) is adjusted in the inversion using the baseline condition variables, producing a posterior baseline (red). During the summer months the proportion of air arriving from the south significantly rises causing a large shift in the posterior baseline relative to the prior baseline calculated from Mace Head data.

Figure 4: Time series of country emission totals 2008-2015. Annual inversion results are given for each gas for three different levels of uncertainty applied to the prior emission map: 100, 1000, and 10,000 times the emissions magnitude for each grid cell. The aggregated country totals from the prior dataset are also given.

Figure 5: The effect of the regridding routine on posterior emission distributions for CF_4. Maps A, C and E are posterior emissions maps at the initial inversion resolution, at 0 regridding steps, at 25 regridding steps and at 50 regridding steps, respectively. Maps B, D, F show the emissions magnitude minus the uncertainty calculated for each inversion grid box at the same regridding levels (0, 25, and 50), which demonstrates the relative uncertainty of the emissions distribution obtained for South Korea. Results are from inversions with initial uncertainty on the prior emissions field set to 100 times emissions at each fine grid square. Units in $Gg\ m^{-2}\ yr^{-1}$.

Figure 6: Emissions maps for all years of data available for CF_4. Results are from inversions with initial uncertainty on the prior emissions field set to 100 times emissions at each fine grid square. Units in $Gg\ m^{-2}\ yr^{-1}$. See Figure S7 for corresponding maps of emissions magnitude minus the uncertainty.

Figure 7: Emissions maps for both years of data available for NF_3: Maps A and C are posterior emissions maps for years 2014 and 2015, respectively. Maps B and D show the emissions magnitude minus the uncertainty calculated for each inversion grid box for years 2014 and 2015, respectively. Results are from inversions with initial uncertainty on the prior emissions field is set to 100 times emissions at each fine grid square. Units in $Gg\ m^{-2}\ yr^{-1}$.

Figure 8: As for Figure 6 but for HFC-23

Tables

795   Table 1: Annual posterior emissions estimates for the five main emitting countries surrounding GSN (Gg yr^{-1}). These posterior emissions estimates are from the inversion that uses a prior emissions uncertainty on each fine grid cell of 100x the prior emission rate.

800

2013

Maximum value = 16.067 s/m

0.003   0.010   0.030   0.100   0.300   1.000   3.000   10.000   30.000

Figure 1

Figure 2

Figure 3

820
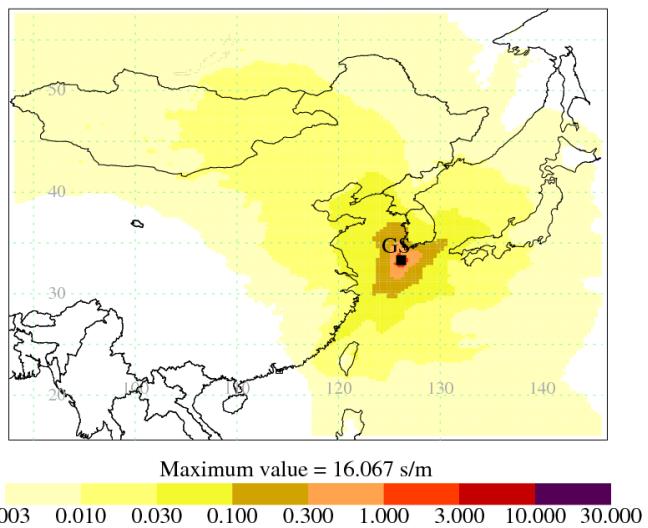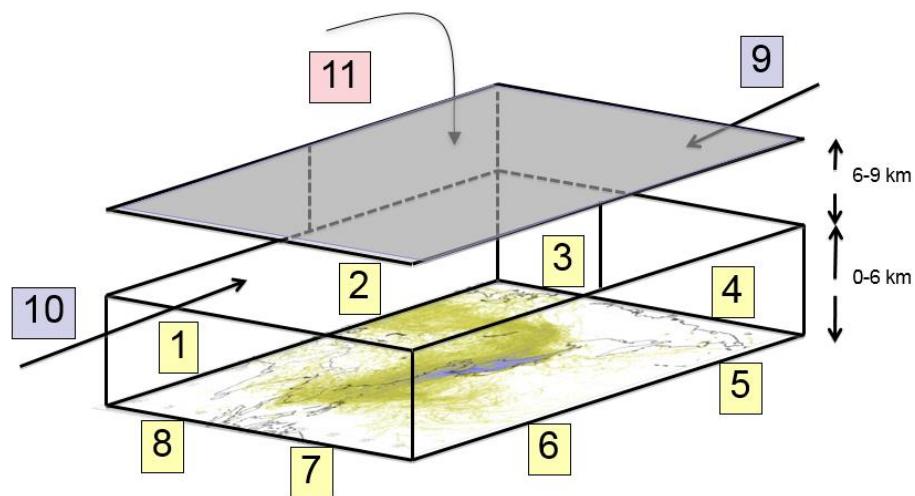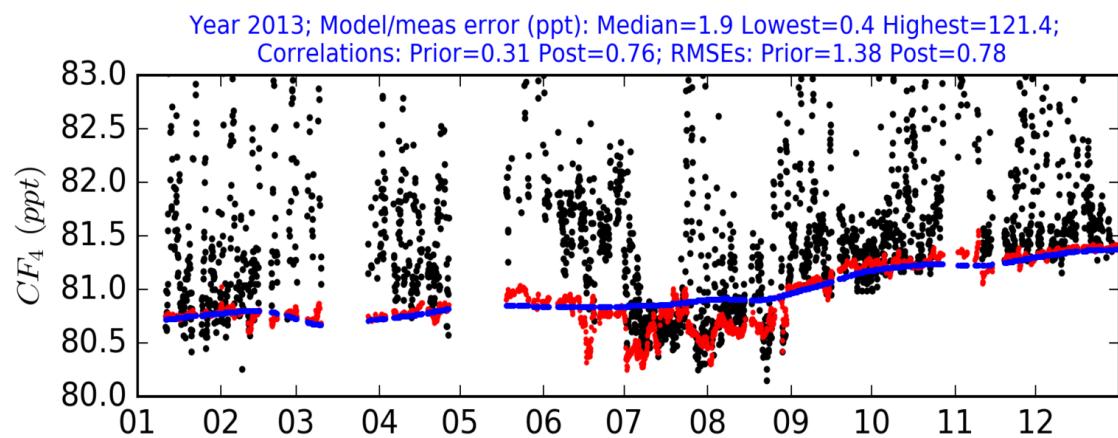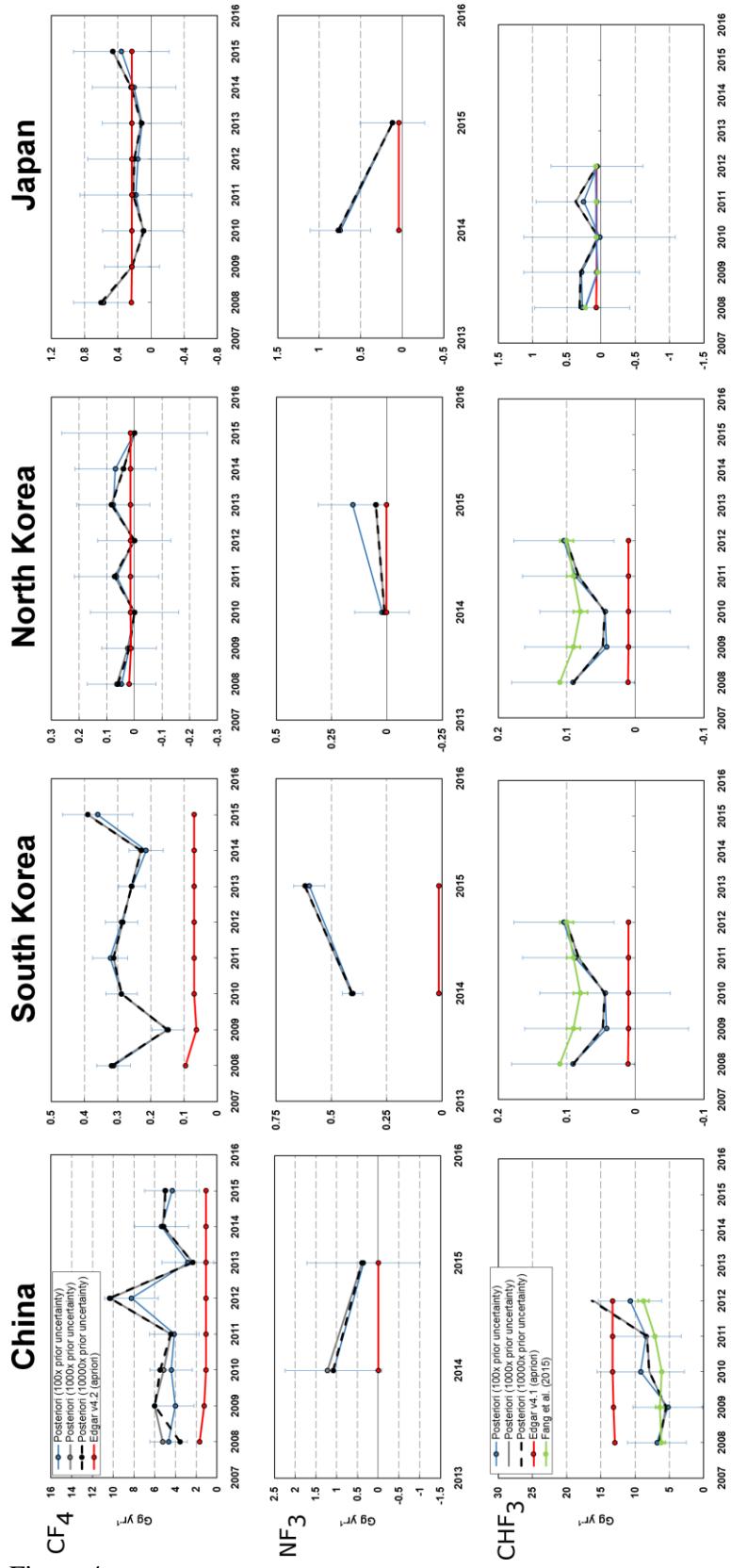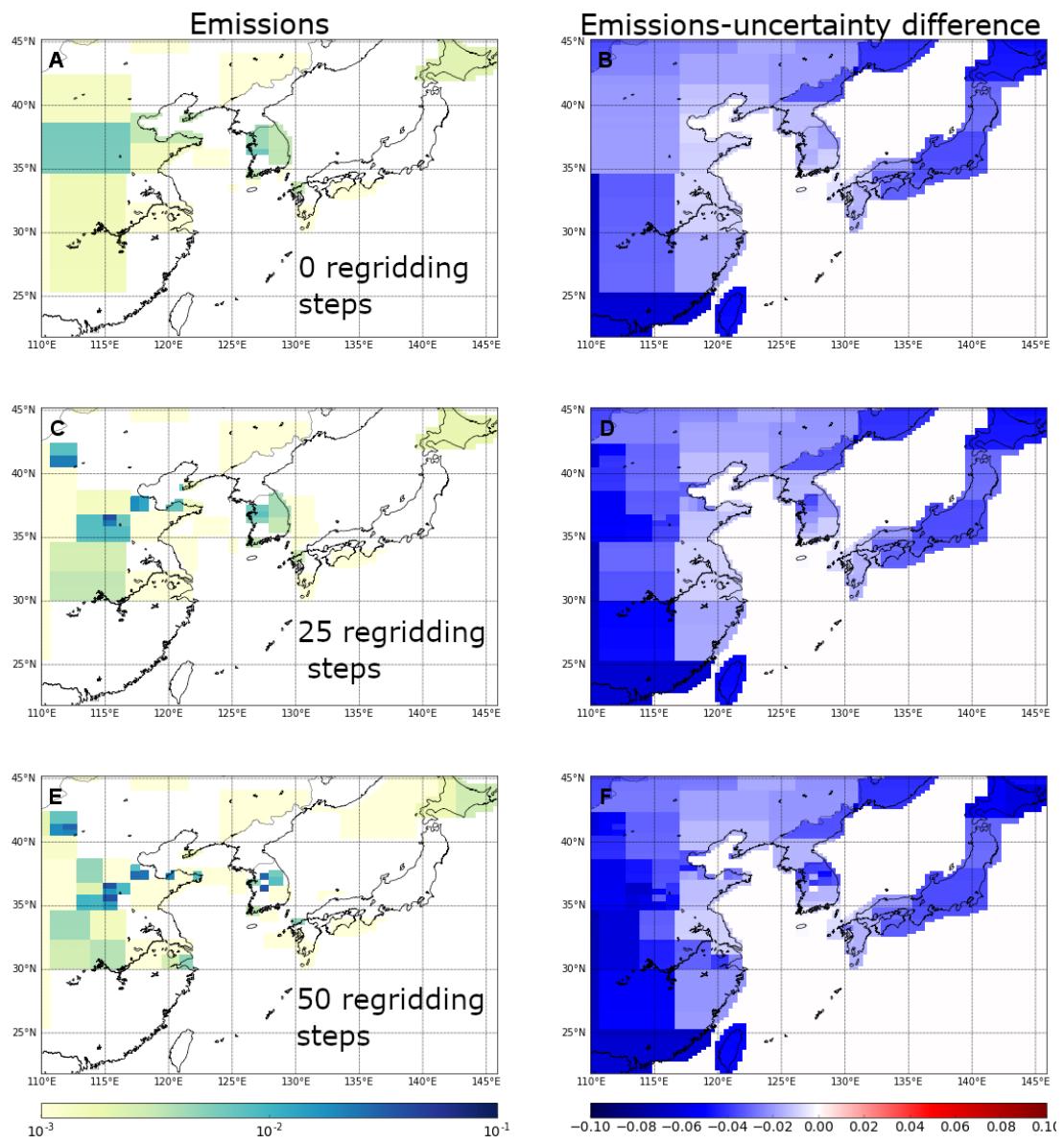
Figure 4

825   Figure 5
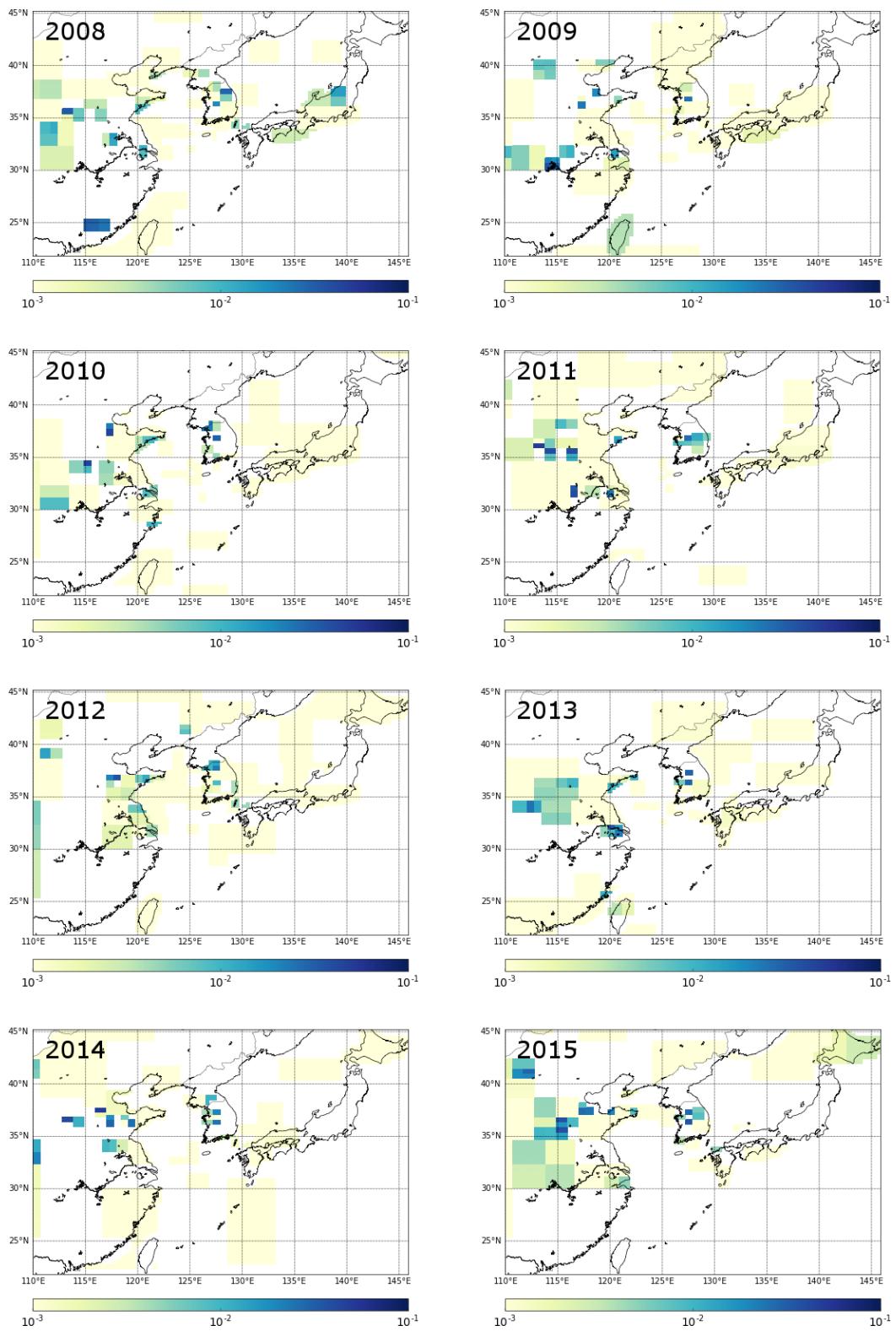
Figure 6
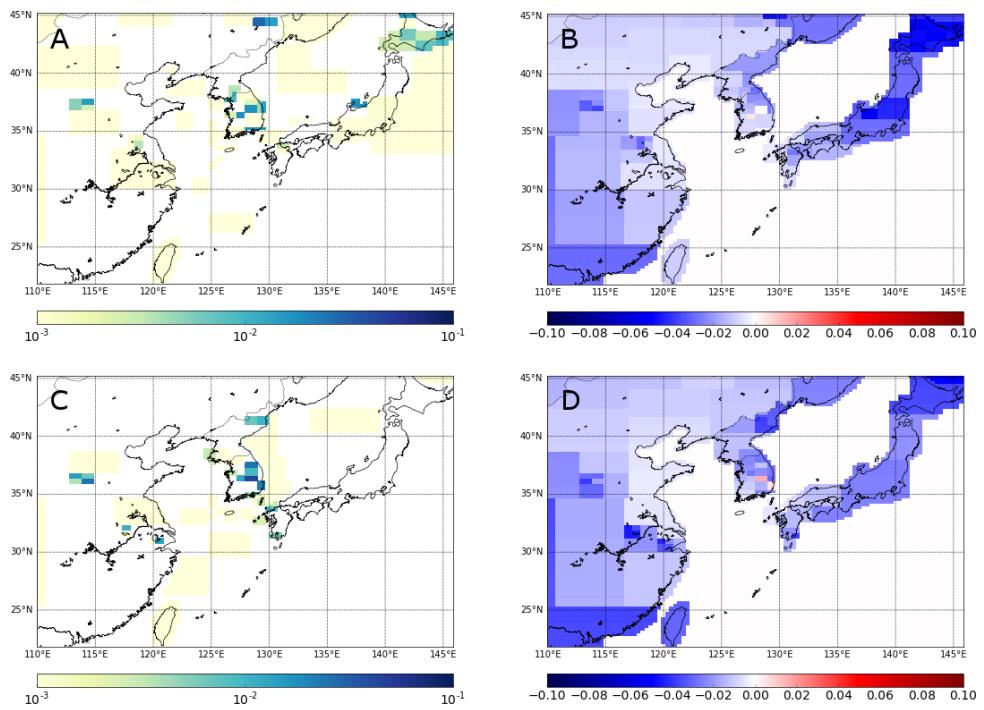
830

Figure: 7
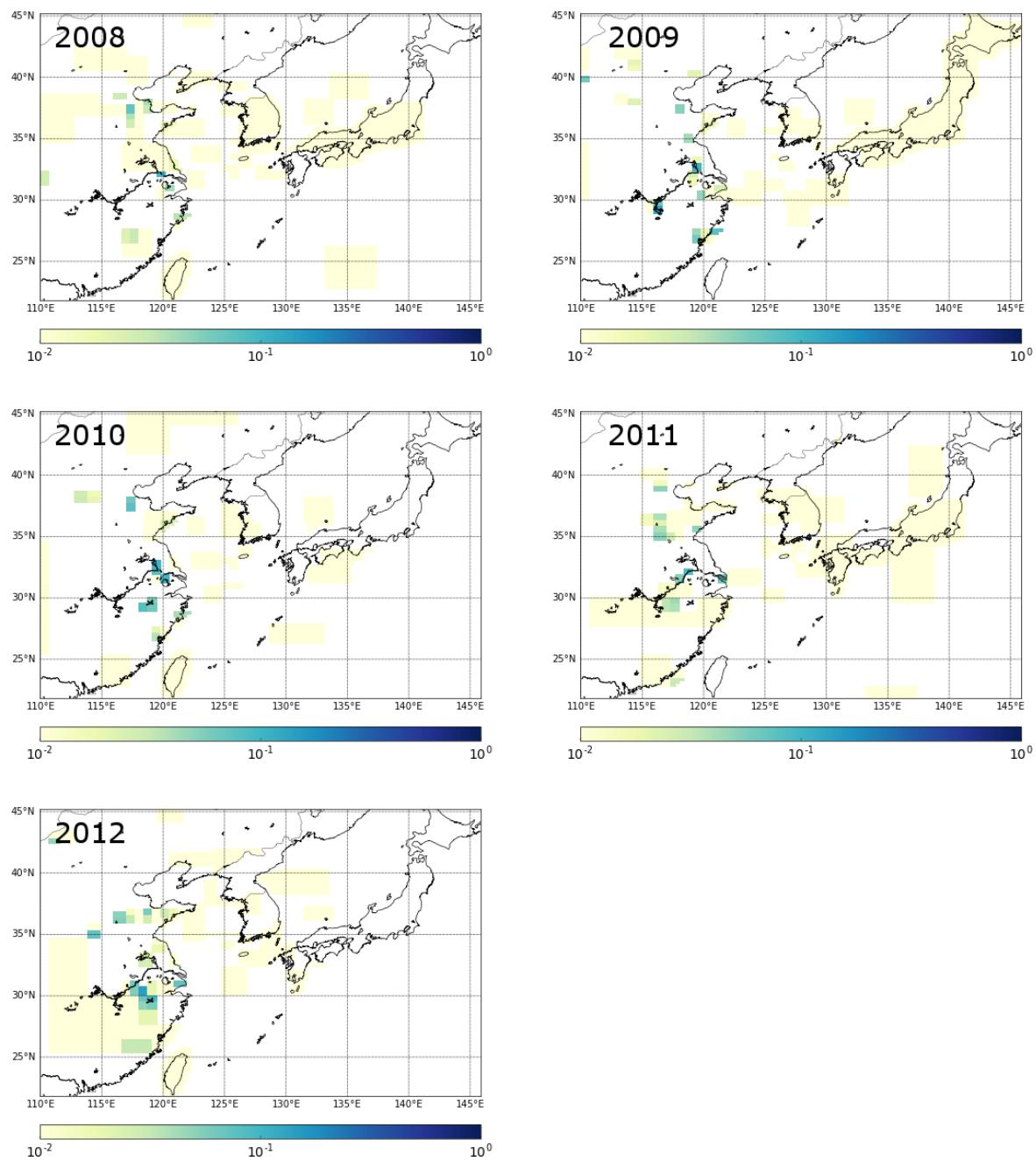
835   Figure 8

	CF$_4$					NF$_3$					HFC-23				
	China	S.Korea	N.Korea	Japan	Taiwan	China	S.Korea	N.Korea	Japan	Taiwan	China	S.Korea	N.Korea	Japan	Taiwan
2008	4.66 (1.82)[#]	0.31 (0.05)[#]	0.05 (0.12)[#]	0.57 (0.36)[#]	0.01 (0.07)						6.8 (4.3)	0.09 (0.09)	0.08 (0.28)	0.28 (0.69)	0.11 (0.15)
2009	4.01 (1.80)	0.15 (0.05)	0.02 (0.10)	0.23 (0.33)	0.32 (0.17)						5.2 (5.1)	0.04 (0.12)	0.00 (0.29)	0.29 (0.84)	0.00 (0.48)
2010	4.42 (2.06)	0.29 (0.05)	0.00 (0.16)	0.10 (0.48)	0.06 (0.13)						9.2 (6.4)	0.04 (0.10)	0.00 (0.39)	0.02 (1.11)	0.00 (0.31)
2011	4.12 (2.37)	0.32 (0.05)	0.06 (0.15)	0.18 (0.67)	0.00 (0.26)						8.4 (5.1)	0.09 (0.08)	0.00 (0.27)	0.26 (0.69)	0.00 (0.41)
2012	8.25 (2.59)	0.29 (0.05)	0.00 (0.13)	0.16 (0.60)	0.04 (0.40)						10.7 (4.6)	0.10 (0.07)	0.00 (0.23)	0.06 (0.67)	0.24 (0.46)
2013	2.82 (2.49)	0.26 (0.04)	0.08 (0.13)	0.11 (0.48)	0.09 (0.26)										
2014	5.35 (2.61)	0.21 (0.05)	0.07 (0.15)	0.21 (0.50)	0.00 (0.30)	1.08 (1.17)	0.40 (0.05)	0.02 (0.12)	0.75 (0.36)	0.03 (0.09)					
2015	4.33 (2.65)	0.36 (0.11)	0.00 (0.26)	0.36 (0.57)	0.00 (0.44)	0.36 (1.36)	0.60 (0.07)	0.15 (0.16)	0.11 (0.39)	0.00 (0.27)					

Kim et al. (2010) estimated CF$_4$ emissions from China in the range 1.7-3.1 Gg yr^{-1} and Li et al. (2011) 1.4-2.9 Gg yr^{-1}. For South and North Korea (combined) Li et al. (2011) estimated emissions of CF$_4$ at 0.19-0.26 Gg yr^{-1} and from Japan at 0.2-0.3 Gg yr^{-1}.

Table 1